 doi:10.20944/preprints202106.0096.v1

Article

Comparison of Direct Intersection and Sonogram Methods for Acoustic Indoor Localization of Persons

Dominik Jan Schott [1]*, Addythia Saphala[2], Georg Fischer[3], Wenxin Xiong[4], Andrea Gabbrielli[1], Joan Bordoy[4], Fabian Höflinger[1], Kai Fischer[3], Christian Schindelhauer[4], and Stefan Johann Rupitsch

[1] Department of Microsystems Engineering, University of Freiburg, Freiburg, Germany
[2] Department of Medical Informatics, Biometry and Epidemiology, Friedrich-Alexander-Universität (FAU), Erlangen, Germany
[3] Fraunhofer Institute for Highspeed Dynamics, Ernst-Mach-Institute (EMI), Efringen-Kirchen, Germany
[4] Department of Computer Science, University of Freiburg, Freiburg, Germany
* Correspondence: dominik.jan.schott@imtek.uni-freiburg.de; Tel.: +49-761-203-7185

Abstract: We discuss two methods to detect the presence and location of a person in a small-scale room and compare the performances. The first method is Direct Intersection, which determines a coordinate point based on the intersection of spheroids defined by observed distances of high-intensity reverberations. The second method, Sonogram analysis, overlays all channel's room impulse responses to generate an intensity map for the observed environment. We demonstrate that the former method has lower computation complexity and higher accuracy for small numbers of channels, while the latter performs more robustly.

Keywords: Presence detection; passive localization; room impulse response; acoustic localization; indoor localization

1. Introduction

ACOUSTIC localization systems outperform the radio-based counterpart in indoor settings, which are not covered by ubiquitous satellite signals of Global Navigation Satellite Systems [1,2]. For some applications, it may not be desirable to equip persons or objects with additional hardware as trackers due to inconvenience and privacy reasons. Previously, we reported coarsely about indoor localization by Direct Intersection in [3]. In this work, we report in detail on two algorithms for this application and their performances. The proposed system is categorized as a passive localization system [4].

Echolocation, such as the method used by bats to locate their prey, is a phenomenon where the reflected sound waves are used to determine the location of objects or surfaces which reflect the sound waves due to a change in acoustic impedance. This concept has been extensively used for various investigations in the physics and engineering fields, such as sound navigation and ranging (Sonar) [5,6].

We draw the approach from bats, which can perceive the incoming reflected wave's direction due to its precise awareness of head angle, body motion, and timing. While the exhaustive echolocation method of bats is not completely understood, one of the more obvious aspects is the back-scattered signals' difference of arrival in time between left and right ears, which can be used to calculate the incoming sound wave's direction [7]. We investigate two different algorithms to interpret the returned signals in a small office room of approximately $3 \times 4 \times 3$ m similar to [8], which are characteristic for the strong multipath fading effects that partially overlap and interfere with the line-of-sight reverberations. Furthermore, we raise the question of the performance of two approaches and compare the memory consumption and execution time.

The detection of more than one person or object is not investigated in this work.

Preprints (www.preprints.org) | NOT PEER-REVIEWED | Posted: 3 June 2021 doi:10.20944/preprints202106.0096.v1

2. Related Work

Indoor presence detection may be achieved through a variety of different technologies and techniques. For one, radio-frequency (RF) based approaches have been implemented. In general, these may be classified into two different employed techniques: received signal strength indicator (RSSI) and radar based approaches. The former offers low-complexity systems with cheap hardware [9], whereas with the latter one, higher accuracy may be achieved [10]. The other main concept employed in indoor presence detection is using the ultrasonic waves, which are applied in active trackers indoors [11,12] and even underwater [13,14].

2.1. RF-RSSI

Mrazovac *et al.* [15] track the RSSI between stationary ZigBee communication nodes, detecting changes to infer a presence from it. In the context of home automation this work is used to switch on and off home appliances. Kosba *et al.* [9] and Retscher and Leb [16] analyze different signal strength features for usability of detection and identification using standard Wi-Fi hardware. Kaltiokallio and Bocca [17] reduce the power consumption of the detection system by distributed RSSI processing.

This technique is then improved by Yigitler *et al.* [18], who build a radio tomographic map of the indoor area. The difference from the previously sampled map of RSSI values is the notification of a presence or occupancy. This general concept is known in the field of indoor localization as fingerprinting. Hillyard *et al.* [19] utilize these concepts to detect border crossings.

2.2. RF-RADAR

Suijker *et al.* [20] present a 24 GHz FMCW (Frequency-Modulated Continuous-Wave) radar system to detect indoor presence and to be used for intelligent LED lighting systems. An interferometry approach is implemented by Wang *et al.* [10] for precise human tracking in an indoor environment.

2.3. Ultrasonic presence detection and localization

A direct approach to provide room-level tracking is presented by Hnat *et al.* [21]. Ultrasonic range finders are mounted above doorways to track people passing beneath. More precise localization can be achieved by using ultrasonic arrays as proposed by Caicedo and Pandharipande [22] [7,22]. The arrays' signals can be used to obtain the range and direction of arrival (DoA) estimates. The system is used for energy-efficient lighting systems. Pandharipande and Caicedo [6] enhanced this approach to track users by probing and calculating the position via the time difference of arrival (TDoA). Prior to that, Nishida *et al.* [23] proposed a system consisting of 18 ultrasonic transmitters and 32 receiver, embedded in the ceiling of a room with the aim to track the aged people and prevent them from accidents. A time of flight (ToF) approach was proposed by Bordoy *et al.* [24], who use a static co-located speaker-microphone pair to estimate human body and wall reflections. Ultrasonic range sensing my be combined with infrared technology, as has been done by Mokhtari *et al.* [25], to increase the energy efficiency.

2.4. Ultrasonic indoor mapping

Indoor mapping and indoor presence detection are two views of the same problem. In both instances one tries to estimate the range and direction for a geometrical interpretation. Ribeiro *et al.* [26] employ a microphone array co-located to a loudspeaker to record the room impulse response (RIR). The multiple reflections can be estimated from this RIR with the use of l_1-regularization and least-squares (LS) minimization, and a room geometry can be inferred, achieving a range resolution of about 1 m. A random and sparse array of receivers is proposed by Steckel *et al.* [27] for an indoor sonar system. In addition to that, the authors use wideband emission techniques to derive accurate three-dimensional (3-D) location estimates. This system is then enhanced with an emitter

Preprints (www.preprints.org) | NOT PEER-REVIEWED | Posted: 3 June 2021 doi:10.20944/preprints202106.0096.v1

array to improve the signal-to-noise-ratio (SNR) [28]. Another approach, implementing a binaural sonar sensor, is proposed by Rajai *et al.* [29]. A sensor was used to detect the wall within a working distance of one meter. In a recent work by Zhou *et al.* [30], it is shown that a single smartphone with the help of a gyroscope and an accelerometer can be used to derive indoor maps by acoustic probing.

2.5. Algorithms

The first set of methods, which are broadly applied are triangulation algorithms as described by Kundu [31]. In this work we focus on two Maximum-Likelihood approaches, similar to the one proposed by Liu *et al.* [32]. The first one, Direct intersection (DI), uses a Look-up-Table (LUT) and Spheres inferred from the sensors delay measurements with error margin. While the other one, the sonogram method, populates a 3-D intensity map with probabilities to find likely positions of the asset. These the approach of the two methods are different, is it likely to expect different outcomes in accuracy, precision, computational complexity as well as memory requirements.

3. System Overview

The system consists of a single acoustic transmitter, a multi-channel receiver, a power distribution board, and a central computer to analyze the recorded signals. Four microphones are placed equidistantly around the speaker and connected to the receiver board. The set-up is shown in Fig. 1, as it is used for the experiment reported below.

3.1. Signal Waveform

Due to their auto-correlation properties and the ability to maximize the Signal-to-Noise-Ratio (SNR) without incrementing the acoustic amplitude, swept-frequency cosine, i.e. frequency modulated chirp signals, perfectly fit our case-study. Auto-correlated frequency modulated chirps are able to provide compressed pulses at the correlator output, which width in time space is defined as follows [33]

$$P_{\mathrm{w}} = \frac{2}{B}. \tag{1}$$

The frequency modulated signal employed in our experiments, $x_{\mathrm{Tx}}(t)$, is mathematically defined as follows

$$s_{\mathrm{tx}}(t) = \begin{cases} A\cos(2\pi\phi(t)), & \text{for } 0 \le t \le T_{\mathrm{s}} \\ 0, & \text{otherwise} \end{cases}, \text{with} \tag{2}$$

$$\phi(t) = \frac{f_{\mathrm{end}} - f_{\mathrm{start}}}{2T_{\mathrm{s}}} t^2 + f_{\mathrm{start}} t, \tag{3}$$

where A denotes the signal amplitude, f_{start} is the start frequency, f_{end} the end frequency, $B = f_{\mathrm{end}} - f_{\mathrm{start}}$ the frequency bandwidth, T_{s} is the pulse duration and $\phi(t)$ the instantaneous phase. The chirp instantaneous frequency is defined as follows

$$f(t) = f_{\mathrm{start}} + \frac{f_{\mathrm{end}} - f_{\mathrm{start}}}{T_{\mathrm{s}}} t, \quad 0 \le t \le T_{\mathrm{s}}. \tag{4}$$

Taking into account the hardware characteristics of our setup, we selected a linear up-chirp pulse with amplitude $A = 1$, $T_{\mathrm{s}} = 5$ ms, $f_{\mathrm{start}} = 16$ kHz, $f_{\mathrm{end}} = 22$ kHz, which result in a time-bandwidth product of $TB = 30$. The frequency response of a chirp signal directly depends on the Time-Bandwidth (TB) product. For chirps with $TB \ge 100$, the pulse frequency response is almost rectangular [34]. However, due to the hardware limitation of our setup, which do not allow to have high (TB) product, the frequency response will be characterized by ripples. In order to mitigate the spectrum disturbances, we window in time domain the transmitted chirp pulse with a raised cosine window [34].

Preprints (www.preprints.org) | NOT PEER-REVIEWED | Posted: 3 June 2021 doi:10.20944/preprints202106.0096.v1

3.2. Hardware overview

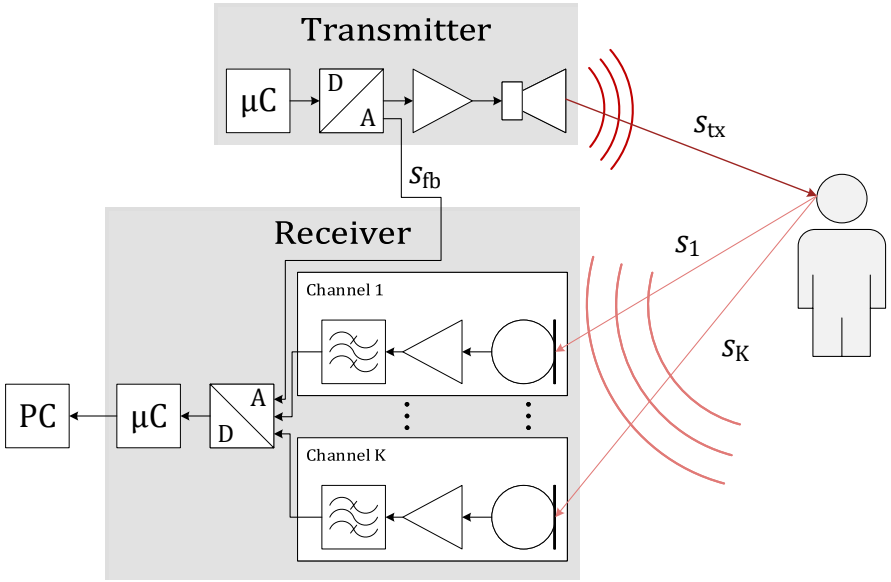

Figure 1. Schematic representation of the system.

To obtain 3-D coordinates with static arrangement, a four-element microphone array is sampled, as well as a feedback signal. This array records the incoming echo wave with different time of arrival, depending on the incoming signal direction. Since unsuitable hardware can affect the system's performance [35], both, microphones and speaker were tested for correct signal generation and reception in an an-echoic box.

3.3. Data acquisition

Each microphone's signal is preconditioned before the digitization by the multi-channel analog-to-digital converter, which was chosen to provide each channel with the identical sample-and-hold trigger flank before conversion. Each frame consist of the signal from each microphone and a feedback, that is recorded as an additional input to estimate and mitigate play-back jitter. The first layer of digital signal processing is to compress the signal, extracting the reverberated acoustic amplitude over time and removing the empty room impulse response (RIR).

3.3.1. Channel phase synchronization

Initially, we calculate the convolution of the feedback channel signal s_{fb} with our known reference signal s_{ref} in its analytic form to obtain the RIR and retrieve the time of transmission from the compressed signal y_{fb}, as shown in eq. 5, where j denotes the imaginary unit.

$$y_{\text{fb}} = |(s_{\text{fb}} \circledast s_{\text{ref}}) + j \cdot \mathcal{H}(s_{\text{fb}} \circledast s_{\text{ref}})| \tag{5}$$

This compressed analytic form y_{fb} of the feedback signal s_{fb} (see Fig. 1 ideally holds only a single pulse from the transmitted signal, if the output stage is impedance matched. Searching for the global maximum returns both, time of transmission, as well as the output amplitude.

$$a_{\text{out}} = \max_{t \to t_0} y_{\text{fb}}(t) \tag{6}$$

In the following, we refer to the start time of a transmission as t_0, all other channels' time scales are regarded relative to t_0. Therefore, the signals of the microphone channels are truncated to remove information prior to the transmission. The ring-down of small office rooms is in the order of 100 ms, so the repetition interval of consecutive transmissions is chosen accordingly larger. This prevents leakage of late echos into the following interval,

Preprints (www.preprints.org) | NOT PEER-REVIEWED | Posted: 3 June 2021 doi:10.20944/preprints202106.0096.v1

that would result in peaks to be recorded after the following interval's line-of-sight. The remaining signal frames from all microphones is compressed with the same approach as the feedback channel, shown in eq. 5 and eq. 6 to extract each channel's compressed analytic signal y_i and line-of-sight detection time t_i.

3.3.2. Baseline removal

In the following we refer to the acoustic channel response after the line-of-sight as the echo profile. An example of such echo profiles is shown in Fig. 2. While the line-of-sight signal ideally provides the fastest and strongest response, large hard surfaces, like desks, walls, and floors return high amplitudes, that are orders of magnitude above a person's echo. For a linear and stable channel, we can reduce this interference from the environment by subtracting the empty room echo profile from each measurement. This profile looses its validity if the temperature changes, the air is moving or objects in the room are moved, e. g. an office chair is slightly displaced. A dynamic approach to create the empty room profile is updating an estimation, when no change is observed for an extended time or alternatively using a very low weight exponential filter to update the room estimation. In this work, the empty office room was sounded N times directly before each test and averaged into an empty room echo profile $\bar{y}_i^\circ$ for each channel i as denoted in eq. 7, to assure unchanged conditions and reduce the complexity of the measurements. The removal itself is then, as mentioned above, the subtracting of the baseline from each measurement, as in eq. 8 under the assumption of coherence.

$$\bar{y}_i^\circ = \text{mean}(y_i^\circ) \tag{7}$$

$$\tilde{y}_i = y_i - \bar{y}_i^\circ \tag{8}$$

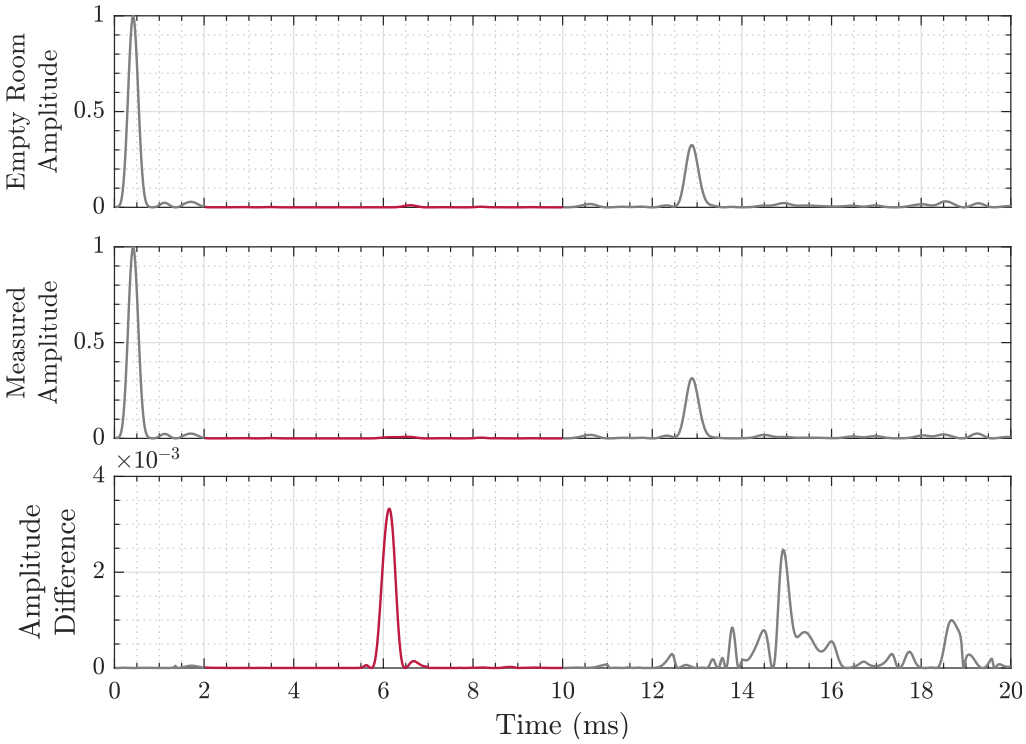

Figure 2. Exemplary magnitude plot of the compressed analytic signal with (**top**) the baseline drawn from an previous recording of the empty room, (**middle**) the room with a person in it, and (**bottom**) the difference of the two above. The red highlighted line in the center marks the area of interest due to geometric constraints. Note the changed scale of the ordinate in the bottom plot.

Preprints (www.preprints.org) | NOT PEER-REVIEWED | Posted: 3 June 2021 doi:10.20944/preprints202106.0096.v1

3.3.3. Time-gating

For our approach we assume some features of the person being closer to the observing system, compared to *distant* environment objects, like chairs, tables and monitors, while another area of reverberations is in the close lateral vicinity of the system, consisting e. g. of lamps and the ceiling. This is exploited by introducing a time gate, that only allows for non-zeros values in the interval of interest as in eq. 9 (also compare Fig. 2).

$$\tilde{y}_{\mathrm{tg,i}} = \begin{cases} \tilde{y}_{\mathrm{i}}, & \text{for } t_{\min} < t < t_{\max} \\ 0, & \text{otherwise} \end{cases} \tag{9}$$

Another assumption is that of a small reverberation area on the person. We assume the points of observation from each microphone to be sufficiently close on a person to overlap. The latter assumption introduces an error, that limits the precision of the system in the order of 10 cm [36], which we deem sufficient for presence detection, as a person's dimension is considerably larger in all directions. This estimation is based on the approximate size of a person's skull and its curvature with respect to the distance to the microphones and their spacing. The closer the microphones and the further the distance between head and device, the more the reflection points will approach each other. If we regard a simplified 2-D projection, where a person with a spherical head of radius $r_{\mathrm{H}} \approx 10\,\mathrm{cm}$ moves in the y-plane only, the position of a reflection point $R = (x_{\mathrm{R}}, z_{\mathrm{R}})$ on the head can be calculated by

$$\begin{aligned} x_{\mathrm{R}} &= x_{\mathrm{C}} - r_{\mathrm{H}} \sin(\alpha_{\mathrm{R}}), \quad \text{and} \\ z_{\mathrm{R}} &= z_{\mathrm{C}} - r_{\mathrm{H}} \cos(\alpha_{\mathrm{R}}), \end{aligned} \tag{10}$$

where x_{C} and z_{C} are the lateral and vertical center coordinates of the head and α_{R} is the reflection angle. The latter is calculated through

$$\alpha_{\mathrm{R}} = \tan^{-1} \frac{x_{\mathrm{C}} + \frac{d_{\mathrm{M}}}{2}}{z_{\mathrm{C}}}, \tag{11}$$

with the distance d_{M} between the microphone and sender. The origin is set to the speaker position. By geometric addition the distance between two such reflection points can be calculated and reach the maximum value if the head moves towards the center. In this case the reflection points would be on the opposing sides of the head and result in a mismatch of $2\,r_{\mathrm{h}}$. The other extreme is laterally moving to a infinite distance, which increases the magnitude of x_{C}, while the distance between microphone and speaker stays constant, therefore the reflection points converge to a single point of reflection. In this work the distance between head center and speaker remained above 120 cm, with a projected error distance of about 1.3 cm.

3.3.4. Echo profile

During the experiment, the reflected signals from the floor, walls, tables and chairs have a very high amplitude. This interference can lead to masking the echo from the target object. To reduce the effect of the interference, the empty room profile is used to subtract the target impulse response from the input impulse response. If we define the reflection from objects other than the target object as noise, we can increase the signal to noise ratio with this method. The empty room impulse response is also called empty room echo profile in this work. In Fig. 2, the upper plot is the empty room impulse response, where the experiment room is cleared of most clutter. The middle plot is the room with single static object as target, shown in Fig. 3. The lower plot shows the result of subtraction between the the second and first plot, the scale is adjusted for clarity purpose.

Preprints (www.preprints.org) | NOT PEER-REVIEWED | Posted: 3 June 2021 doi:10.20944/preprints202106.0096.v1

3.3.5. Distance maps

Look-up tables are calculated before the experiment to estimate the travel distance of a signal from the speaker to each microphone under the assumption of a direct reverberation from a point at position $\vec{x}$ in the room and linear beam-like signal propagation. This grid is formed by setting the center speaker as origin and spanning up a 3-dimensional Cartesian coordinate system of points $\vec{x}$ through the room in discrete steps. We limit the grid to the intervals X_1 to X_3 in steps of 1 cm to decrease the calculational effort and multipath content under the prior knowledge of the rooms geometry as follows:

$$\begin{aligned} \vec{x} &= (x_1, x_2, x_3) \in \mathbb{X}, \text{ where} \\ \mathbb{X} &= \{X_1 \times X_2 \times X_3\} \subset \mathbb{R}^3. \end{aligned} \tag{12}$$

The look-up table approach serves to minimize the processing time during execution. The distance maps provide pointers to convert from binary sampling points to distance points. Each sub-matrix contains the sum of distance between each point in the room to the corresponding i^{th} microphone at the position $\vec{x}_{\mathrm{M,i}}$ and to the speaker at position $\vec{x}_{\mathrm{S}}$, which cover the flight path of the echoes, as in eq. 13:

$$M_{\mathrm{i}}(\vec{x}) = \|\vec{x} - \vec{x}_{\mathrm{S}}\| + \|\vec{x}_{\mathrm{M,i}} - \vec{x}\|. \tag{13}$$

Therefore, the resultant entries in matrices M depend on the geometric arrangement of speaker and microphones, and the matrix size corresponds to the area of detection, as in eq. 12.

3.4. Data processing

3.4.1. Direct Intersection

The main assumption for this approach is, that the highest signal peak in the observation window of each channel is indicating the position of interest, as visualized in Fig. 2. Each channels' peak index defines the radius r_{i} of a sphere around each microphone, which is contained in the point cloud L_{i}. While ideally those spheres overlap in exactly the point of reverberation, in practical application, where noise, interference and jitters are present, this is not the case. To compensate this error, we pad the sphere by Δr additional points in radius until all spheres overlap and the unity of valid estimation points U_{L} is not empty. The sphere radius widening Δr can be used as an indication of each measurements quality, as a low error case will require little to no padding, while in high error cases, the required padding will be large. Another approach is to use a fixed and small padding, which will ensure only measurements of high quality to be successful, but will fail for high error scenarios.

3.4.2. Sonogram

The Sonogram approach leverages available memory and processing power to build a 3-D intensity map. This approach utilizes the entire echo profile difference shown in Fig. 2 (bottom) and map them into the 3-D distance map explained in section 3.3.5, with the assumption that the highest peak correspond to the source of reverberation. The multiplication of impulse amplitude that correspond to the same coordinates are used as an indication of possible reverberation source. Therefore, the maximum result would have the highest likelihood of being the reverberation source location.

Preprints (www.preprints.org) | NOT PEER-REVIEWED | Posted: 3 June 2021 doi:10.20944/preprints202106.0096.v1

Algorithm 1: Direct Intersection Estimation

Input : $\tilde{y}_{\mathrm{tg}}$, observed intensity data frames,
M_{i}, distance maps,
K, number of channels,
$\Delta r_{\max}$, maximum radius spreading distance.
Output: $\vec{x}_{\mathrm{est}}$, estimated 3D-position.

begin
- $\Delta r \leftarrow 0$ // initial estimation tolerance
- $N_{\mathrm{OL}} \leftarrow 0$ // number of overlapping points
- **for** $i = 1$ **to** K **do**
  - $r_{\mathrm{i}} \leftarrow \max_{n \to r_{\mathrm{i}}} \tilde{y}_{\mathrm{tg}}$ // get index of peak
  - $R_{\mathrm{i}} \leftarrow \{r_{\mathrm{i}}\}$
- **while** $(N_{\mathrm{OL}} = 0)$ & $(\Delta r < \Delta r_{\max})$ **do**
  - $\Delta r{+}{+}$
  - **for** $i = 1$ **to** K **do**
    - $R_{\mathrm{i}} \leftarrow \{r_{\mathrm{i}} - \Delta r,\ R_{\mathrm{i}},\ r_{\mathrm{i}} + \Delta r\}$ // recursively add width
    - $L_{\mathrm{i}} \leftarrow \mathrm{isMember}(M_{\mathrm{i}},\ R_{\mathrm{i}})$ // select points by radius [37]
  - $U_{\mathrm{L}} \leftarrow (L_1\ \&\ \ldots\ \&\ L_{\mathrm{K}})$
  - $\vec{x}_{\mathrm{OL}} \leftarrow \mathrm{ind2sub}(\mathrm{size}(U_{\mathrm{L}}), \mathrm{find}(U_{\mathrm{L}}))$ // wrap into 3-D coordinates [38]
  - $N_{\mathrm{OL}} \leftarrow \min(\mathrm{length}(\vec{x}_{\mathrm{OL}}))$
- $\vec{x}_{\mathrm{est}} = \mathrm{mean}(\vec{x}_{\mathrm{OL}})$

Algorithm 2: Sonogram Estimation

Input : $\tilde{y}_{\mathrm{tg}}$, observed intensity data frames,
M_{i}, distance maps,
K, number of channels,
$\Delta r_{\max}$, maximum radius spreading distance.
Output: $\vec{x}_{\mathrm{est}}$, estimated 3D-position.

begin
- $\tilde{y}_{+} \leftarrow \{\tilde{y}_{\mathrm{tg}} > 0\}$ // remove negative intensities
- **forall** $\vec{x}$ **do**
  - $I(\vec{x}) \leftarrow \prod_{i=1}^{K} \tilde{y}_{+,\mathrm{i}}(M_{\mathrm{i}}(\vec{x}))$
- $A_{\mathrm{x1}} \leftarrow \max_{x_1 \in X_1}(I)$ // 2D matrix
- $\vec{a}_{\mathrm{x2}} \leftarrow \max_{x_2 \in X_2}(A_{\mathrm{x1}})$ // 1D vector
- $x_{3,\mathrm{est}} \leftarrow \max_{x_3 \in X_3}(\mathrm{smooth}(\vec{a}_{\mathrm{x2}}))$ // scalar, moving average smoothed [39]
- $x_{2,\mathrm{est}} \leftarrow \mathrm{find}(\vec{a}_{\mathrm{x2}},\ x_{3,\mathrm{est}})$ // select first matching value [40]
- $x_{1,\mathrm{est}} \leftarrow \mathrm{find}(A_{\mathrm{x1}},\ \{x_{2,\mathrm{est}}, x_{3,\mathrm{est}}\})$
- $\vec{x}_{\mathrm{est}} \leftarrow (x_{1,\mathrm{est}},\ x_{2,\mathrm{est}},\ x_{3,\mathrm{est}})$

Preprints (www.preprints.org) | NOT PEER-REVIEWED | Posted: 3 June 2021 doi:10.20944/preprints202106.0096.v1

4. Experiments

4.1. Set-up

In the experiment, we use a mock-up representing a person's head as the experiment target. The hard and smooth surface of the object is intentional for the sake of usability and to remove unintended movements from our measurements at this early stage. In the set-up shown in Fig. 3 the central speaker emits the well-known signal s_{tx}, the reflected echoes from the target s_1 to s_4 are recorded by the microphone array around the speaker. The depiction in Fig. 3 is exaggerated for clarity.

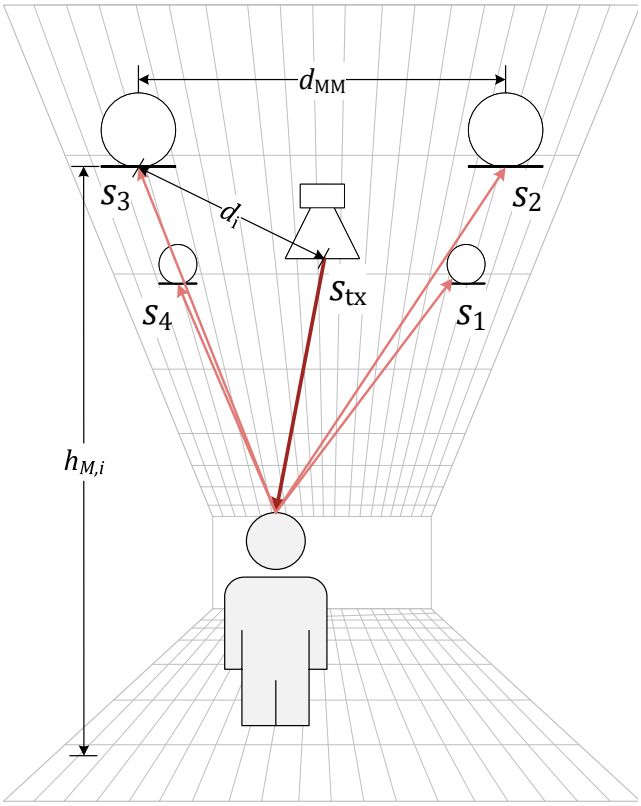

Figure 3. Experimental Set-up for $K = 4$ receivers spaced by $d_{\text{MM}} \approx 0.2\,\text{m}$. The transmitted signal s_{tx} is observed as reflected signals s_{i} by the system located near the ceiling of the room.

Table 1 shows the spherical coordinates of the target inside the room, with the center of the device as the reference point. The device is positioned on the ceiling, oriented downward. For each position we measure the distance for the assumed acoustic path with a laser distance meter `Leica DISTO`$^{\text{TM}}$ `D3a BT` for reference. As mentioned above, the coordinate system's point of origin is set to the center of the device, the x-axis is set perpendicular to the entrance door's wall (bottom of Fig. 5) and increasing towards the right, the y-axis is parallel to the line of sight from the door and increasing towards the rear end of the room, and the z-axis is zero in the plane of the device (upper ceiling lamp level) and decreasing towards the floor. The measured reference positions of the measurement dummy are listed in Tab. 1 and indicated by the green diamond in Fig. 5, 5, 9, and Fig. 9. The two dimensional depictions are shown in Cartesian coordinates to provide clarity, while the detection results are done in spherical coordinates.

Preprints (www.preprints.org) | NOT PEER-REVIEWED | Posted: 3 June 2021 doi:10.20944/preprints202106.0096.v1

Table 1. Reference Positions

Pos.	r (m)	θ (°)	ϕ (°)
①	1.58	77	59
②	1.70	-92	57
③	1.23	-35	54
④	1.26	169	54

4.2. Empty room profile

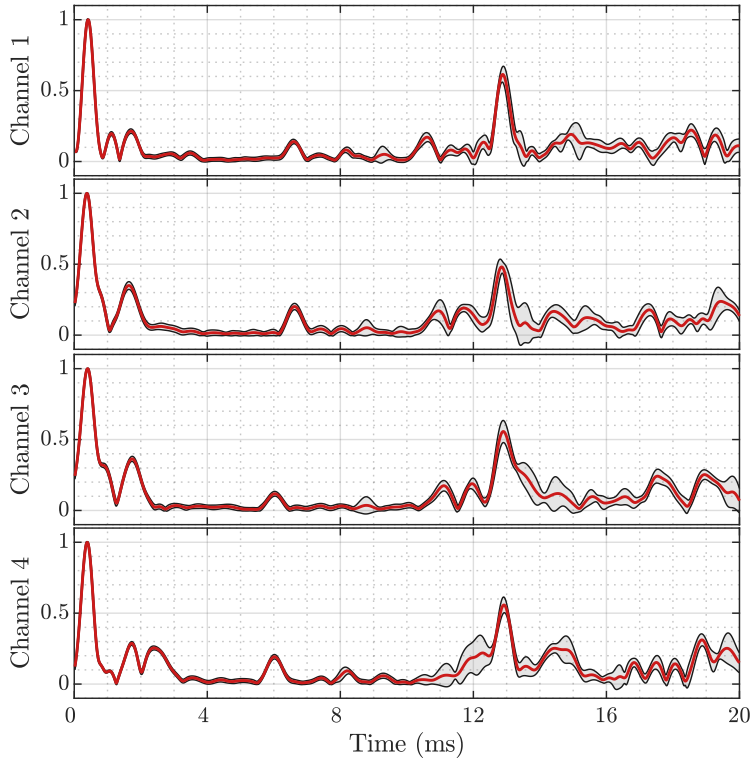

Figure 4. Response of the empty room for all 4 channels s_1 to s_4. The red line indicates the mean response over 100 measurements, the grey envelope the $\pm 3\sigma$ region. The first peak marks the line-of-sight arrival time and is used for time synchronization.

Similar to the later experiments we sound the room 100 times as described in Ch. 3.3.2 to record the baseline profiles shown in Fig. 4. This recordings are taken one time and serve for reference for all later experiment runs. During the recordings the room was left closed and undisturbed. The recordings still show significant variances in each channel at varying positions, e.g., as shown in the uppermost subplot of Fig. 4 from 15 to 16 ms. Below 8 ms this intervals with increased variances do not occur, indicating a stable channel. The signals' interval close to zero contains strong wall and ceiling echos. Note the very strong reverberation peak at 12.5 to 13.5 ms that is caused by the floor. As our area of interest does not fall in this distance, we omit it for analysis as well. Hence the time-gate limits as introduced in Ch.3.3.3 are $t_{\text{min}} = 3\,\text{ms}$ and $t_{\text{max}} = 8\,\text{ms}$.

4.3. Results

4.3.1. Direct Intersection

The localization by Direct Intersection from all 100 runs is shown for each of the 4 reference positions in Fig. 5 and 5. While the statistical evaluation is performed in spherical coordinates due to the geometric construction during the estimation, this overview plots, as well as those for the Sonogram localization are drawn in Cartesian

Preprints (www.preprints.org) | NOT PEER-REVIEWED | Posted: 3 June 2021 doi:10.20944/preprints202106.0096.v1

coordinates that allow for easier verification and intuitive interpretation. The lateral spread of the estimation point cloud in Fig. 5a is misleading as the points are situated on a sphere around the origin. The projected lateral extend is almost entirely due to the angular errors.

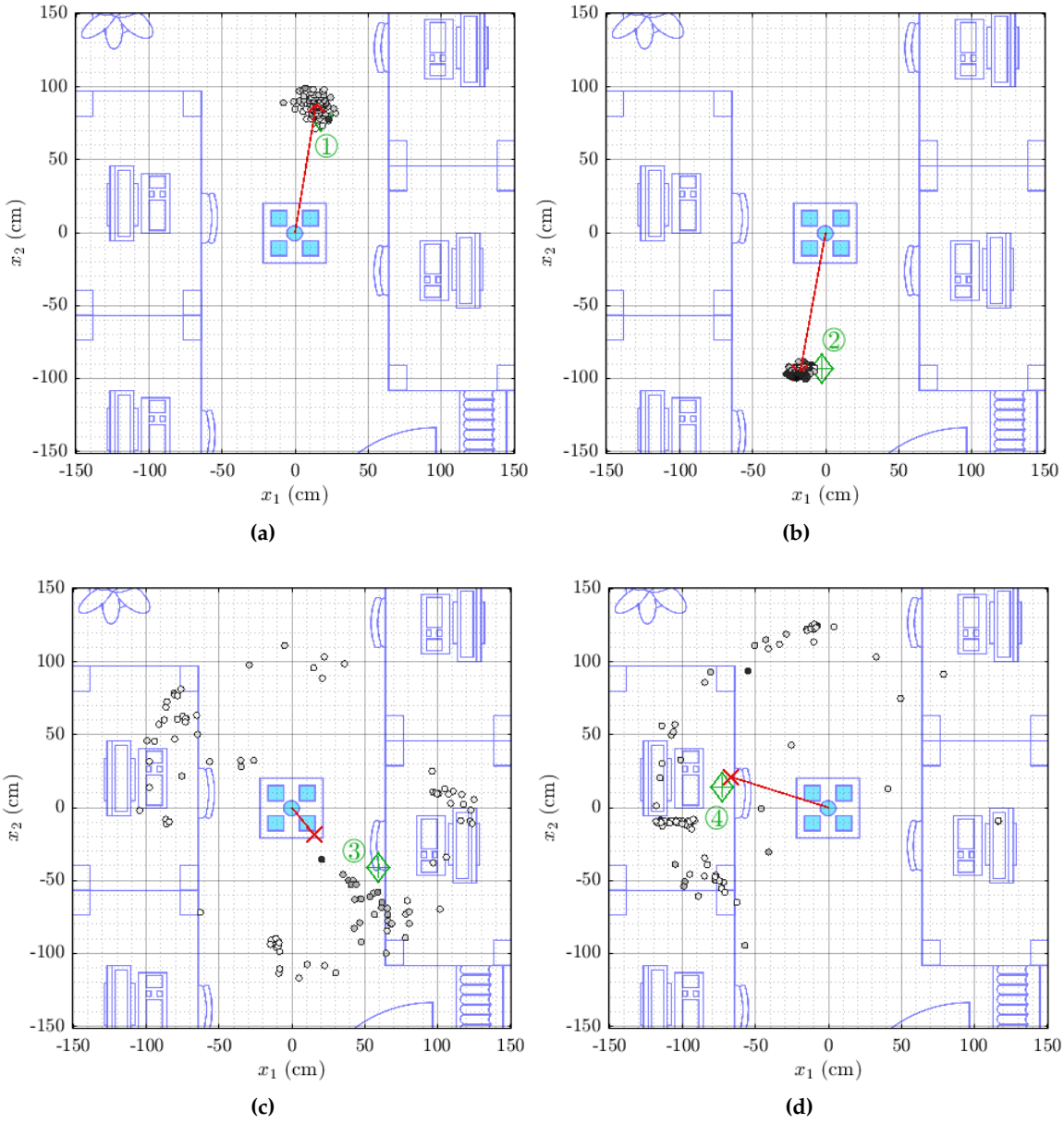

Figure 5. 2D-Projection of 100 estimations of 3D-positions ① (**a**), ② (**b**) ③ (**c**) and ④ (**d**) by Direct Intersection. The single estimations are indicated by the black circled markers, the red cross marks the Carthesian averaged position and is highlighted by the red line to the origin, and the green diamond indicates the reference position. The points' infill is proportional to the observed intensity relative to the radius spreading (darker is higher).

Positions ① and ② show a distance estimation deviation of $\sigma_r \approx 10\,\text{cm}$, as well as azimuth and elevation angle errors of $\sigma_\text{ϟ} \approx \sigma_\text{ϱ} < 5°$ for both, Direct Intersection and Sonogram localization (compare Tab. 2 and 3. For positions ③ and ④, which are situated closer to the desks, the deviation increases to almost 40 cm in distance and almost arbitrary azimuth angles with a $\sigma_\text{ϟ} \approx 120°$ and more, but a far less affected elevation angle estimation with a $\sigma_\text{ϟ} < 10°$. The deviations are calculated around the

Preprints (www.preprints.org) | NOT PEER-REVIEWED | Posted: 3 June 2021 doi:10.20944/preprints202106.0096.v1

mean estimator for each value. For simplicity of interpretation, the mean error for each dimension is shown in Tab. 4.

Table 2. Direct Intersection Estimated Positions

Pos.	r (m)	θ (°)	ϕ (°)
①	1.83 ± 0.14	81 ± 4	61 ± 1
②	2.01 ± 0.11	-100 ± 3	61 ± 1
③	1.92 ± 0.37	4 ± 96	59 ± 4
④	2.12 ± 0.25	-58 ± 135	60 ± 3

The error distributions for each dimension are shown in Fig. 6, where each column depicts one of the spherical dimensions (radius, azimuth angle and elevation angle), while each row represents the results from the reference position indicated to the left of the plot. For the first two positions the distributions are almost unimodal, but for the latter two this does not hold true, making the mean value and standard deviation unsuitable estimators.

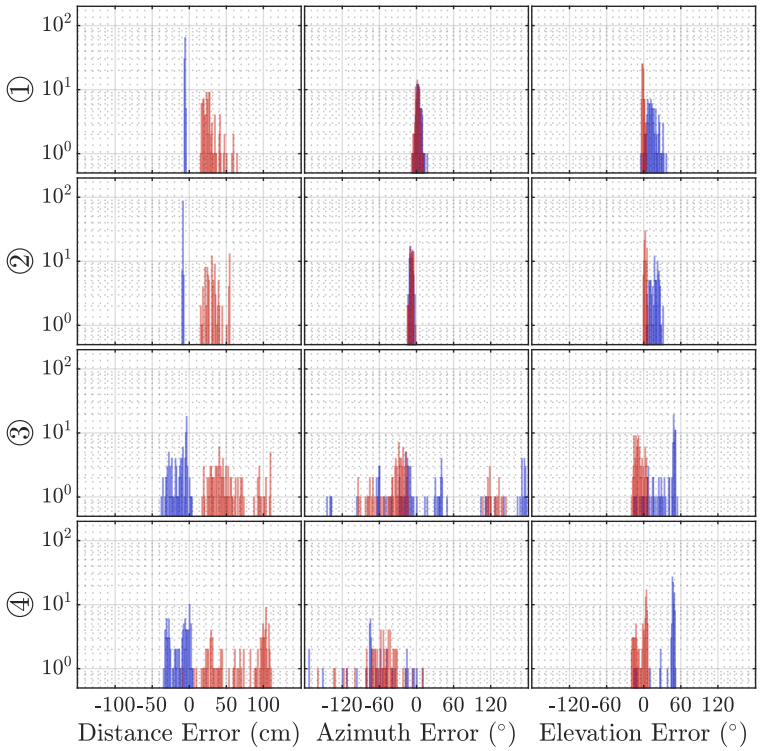

Figure 6. Histograms of the error in estimation compared to the reference over 100 localization repetitions at each position by DI (blue) and Sonogram (red) estimation. Each row depicts the 3 degrees of freedom for each position.

The distribution of the error in the absolute distance between the estimated positions and reference positions (see Fig. 7) is likewise a few dozen centimeters for the first two cases, but around 1 m for the latter two. If we recall the reference positions from Tab. 1, the true distances are between 1 m to 2 m, which puts the error in the same order as the expected value.

The Direct Intersection method allows for an investigation into the time variance of the detected maximum peak which is depicted in Fig. 8. In the first two cases we observe unimodal distributions of around 10 samples in width, while the latter cases show detected peaks all over the interval.

Preprints (www.preprints.org) | NOT PEER-REVIEWED | Posted: 3 June 2021 doi:10.20944/preprints202106.0096.v1

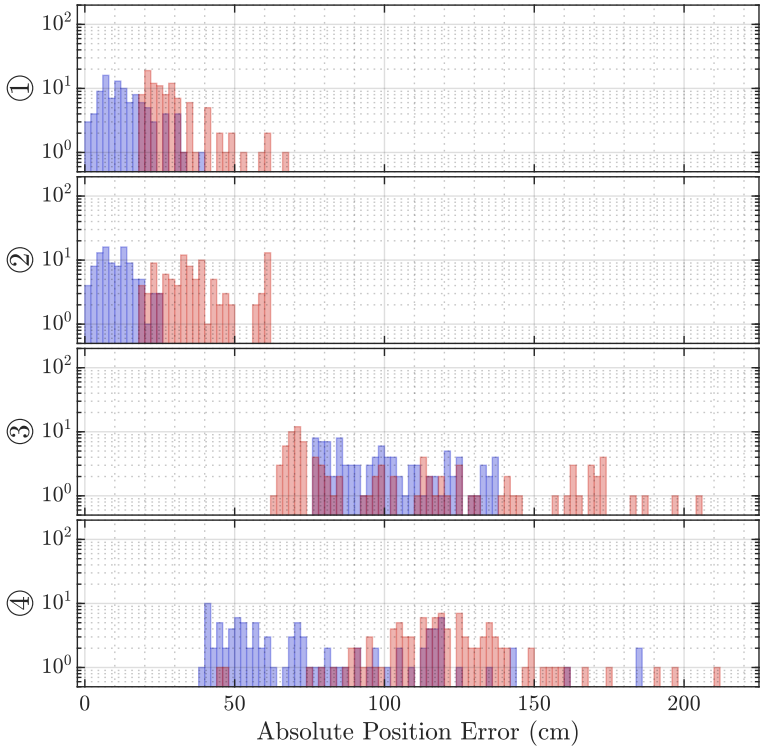

Figure 7. Histograms of the absolute distance error in estimation compared to the reference over 100 localization repetitions at each position by DI (blue) and Sonogram (red). Each row depicts the 3 degrees of freedom for each position.

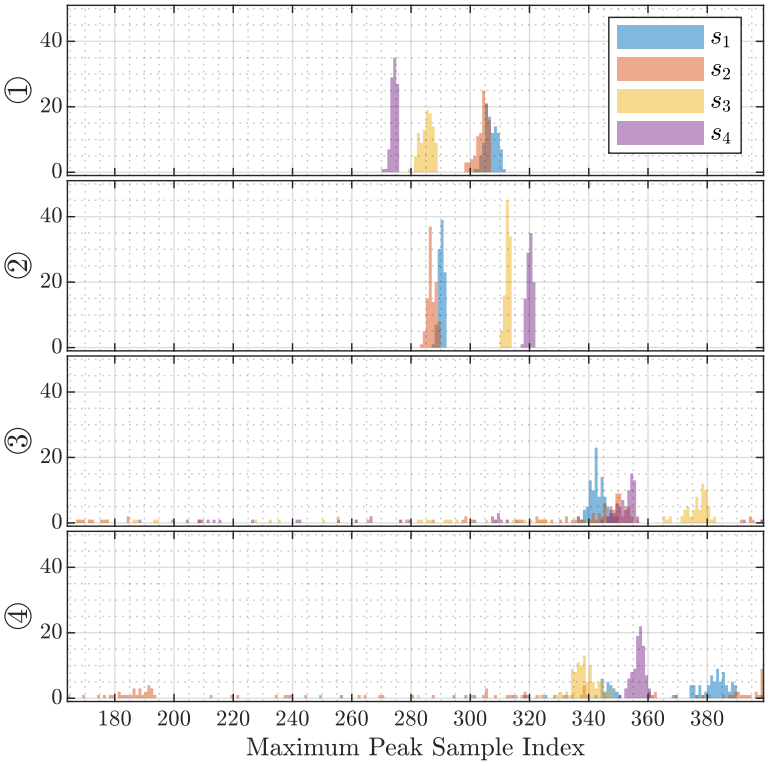

Figure 8. Histograms of the highest peak position of each microphone's channel over 100 localization repetitions at each position by DI. Each row depicts the 3 degrees of freedom for each position.

Preprints (www.preprints.org) | NOT PEER-REVIEWED | Posted: 3 June 2021 doi:10.20944/preprints202106.0096.v1

4.3.2. Sonogram

The Sonogram localization on the same data as before in Ch. 4.3.1 is shown in Fig. 9 and 9 for all 4 cases. The lateral distribution of the estimated locations is not following the spherical shape as closely as is the case for those by Direct Intersection estimations (compare e.g., Fig. 5a).

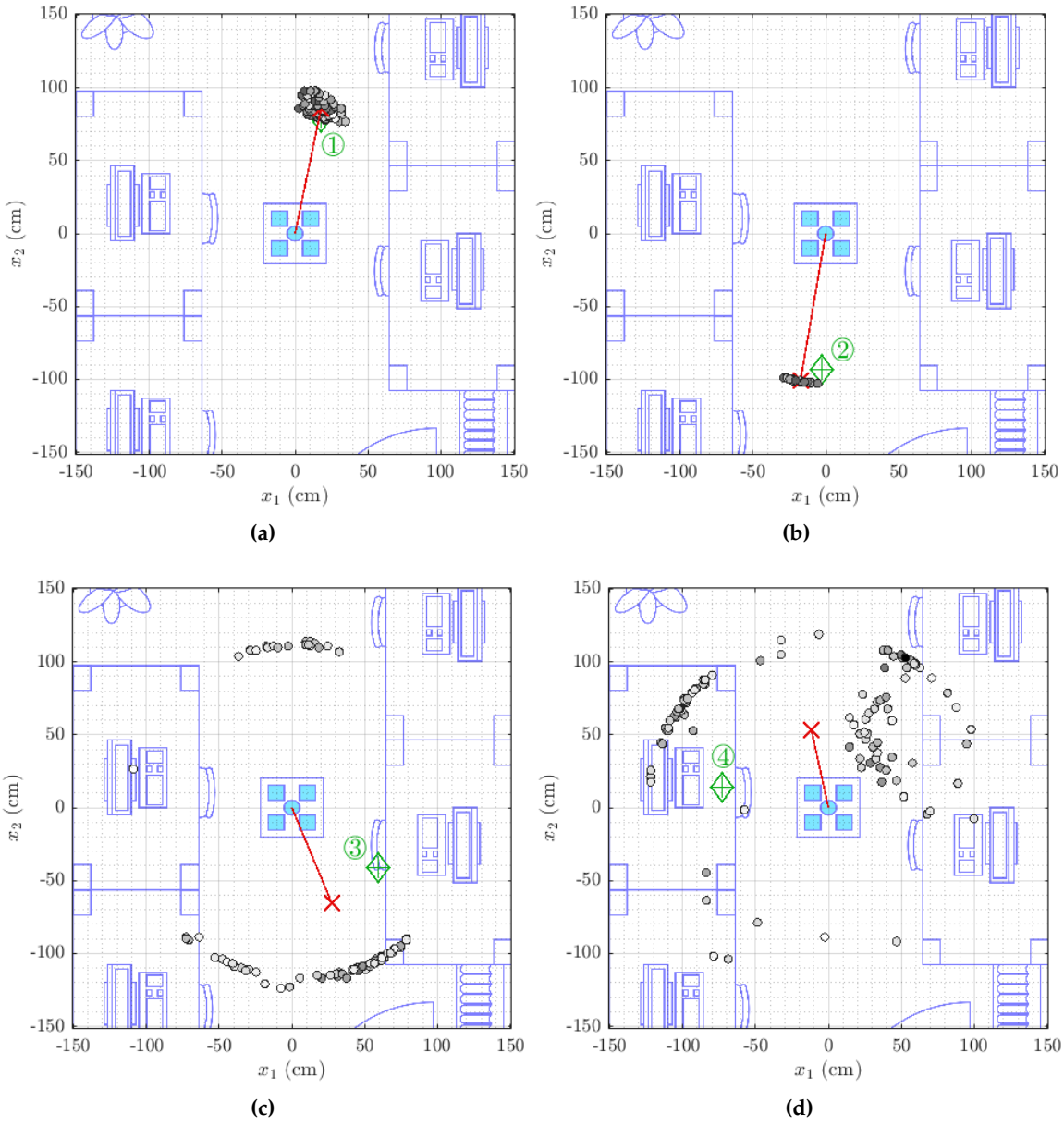

Figure 9. The same plot as in Fig. 5 for positions ① (**a**), ② (**b**), ③ (**c**) and ④ (**d**) but by Sonogram. The point's infill is proportional to the observed intensity.

Similar to before, the method performs well in the first two cases, exhibiting small deviations (see Tab. 3), but far less precise with the largest deviation increase in the azimuth angle, too. The corresponding mean errors to the reference positions are listed in Tab. 4.

Preprints (www.preprints.org) | NOT PEER-REVIEWED | Posted: 3 June 2021 doi:10.20944/preprints202106.0096.v1

Table 3. Sonogram Estimated Positions

Pos.	r (m)	θ (°)	ϕ (°)
①	1.85 ± 0.10	80 ± 4	58 ± 2
②	2.03 ± 0.11	-100 ± 3	60 ± 2
③	1.77 ± 0.26	-41 ± 69	47 ± 7
④	1.96 ± 0.34	31 ± 119	51 ± 9

Table 4. Mean Error for Direct Intersection and Sonogram

	Direct Intersection			Sonogram		
Pos.	r (m)	θ (°)	ϕ (°)	r (m)	θ (°)	ϕ (°)
①	0.25	3	2	0.27	2	1
②	0.31	8	4	0.34	8	3
③	0.69	39	5	0.53	6	7
④	0.87	47	6	0.70	138	3

The cases ③ and ④ display two larger clusters of estimated positions, which leads to the bimodal error distributions in Fig. 6.

The absolute error is similarly distributed around lower values for the former two cases and widely spread for the two latter cases (see Fig. 7). Note that the error distribution plots for the Sonogram are of slightly different horizontal scale, as no errors below 20 cm were observed, while the observed maximal error exceeds 200 cm.

Lastly, the performance of both algorithms with regard to execution time is listed in Tab. 5 and mean required memory in Tab. 6. The distribution of those measures is shown in Fig. 10 and Fig. 11. The Direct Intersection method requires roughly 2.4× less memory than the Sonogram localization. With a best case mean execution time of 0.66 s the former algorithm is almost 1.7× faster than the best case mean of the latter method, while the worst case mean - almost unchanged for the Sonogram approach - is with a factor of 7.1 for the Direct Intersection by far slower than the worst case mean execution time of the Sonogram method.

Table 5. Runtime Performance: Time

	Direct Intersection	Sonogram
Pos.	Time (s)	Time (s)
①	0.94 ± 0.17	1.14 ± 0.07
②	0.66 ± 0.13	1.20 ± 0.02
③	6.38 ± 6.60	1.10 ± 0.01
④	8.58 ± 7.12	1.10 ± 0.01

Table 6. Runtime Performance: Memory

Direct Intersection	Sonogram
Memory $(\times 10^8\,\text{bit})$	Memory $(\times 10^8\,\text{bit})$
1.600 ± 0.004	3.840 ± 0.002

Preprints (www.preprints.org) | NOT PEER-REVIEWED | Posted: 3 June 2021 doi:10.20944/preprints202106.0096.v1

The Direct Intersection execution time varies strongly, as we observe it anywhere between 0.25 s and 25.0 s, thus, without further limitations, does not allow for a well confined prediction of the localization algorithm's execution time.

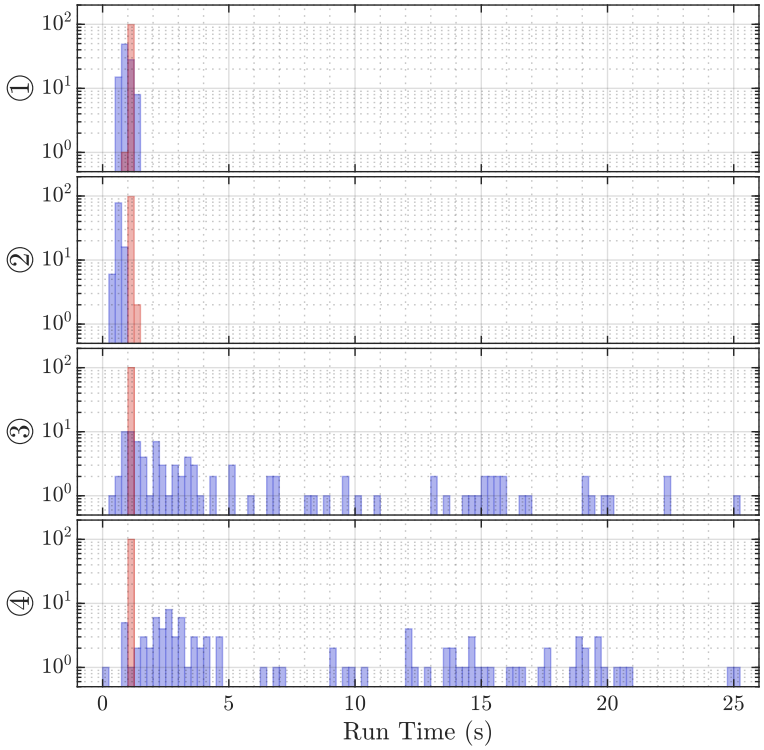

Figure 10. Histograms of the execution time of 100 localization repetitions at each position by DI (blue) and Sonogram (red).

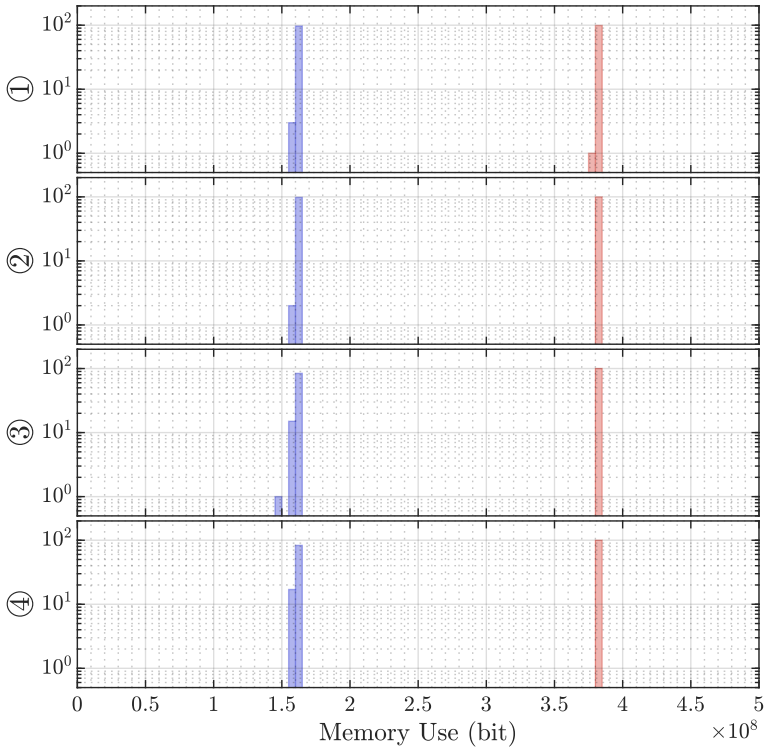

Figure 11. Histograms of the memory allocation during 100 localization repetitions at each position by DI (blue) and Sonogram (red).

Preprints (www.preprints.org) | NOT PEER-REVIEWED | Posted: 3 June 2021 doi:10.20944/preprints202106.0096.v1

5. Discussion

5.1. Localization

The Direct Intersection method provides throughout all cases distance estimations, that are too short, while the Sonogram based localization returns distance estimations that are longer than the reference (compare Fig. 6). Regarding the absolute error distribution, we observe that the Direct Intersection method performs more accurate, especially in the better cases ① and ②, as well more precise in the first three of the four observed cases, as drawn from Fig. 7. Possible cause of the degradation of both methods performance for cases ③ and ④ is in the peak detection algorithm, as Fig. 8 shows a wide error range of detected possible peaks. While this was observed specifically for the Direct Intersection method, this also implies the low signal-to-noise ratio of the underlying echo profile, and consequently also affects the Sonogram estimation. Interestingly, the lower estimation errors for cases ① and ② implicate a better performance for the larger distances than the closer ones, which is counter-intuitive from a power perspective, but if we recall the empty room impulse responses shown in Fig. 4, where noise is included as the curves' variance and compare it to the magnitudes of a person's signal in Fig. 2, the difference in magnitude is in the same order. For higher distances the variance increases, as fluctuations in the speed of sound cause phase distortions, but for lower distances interference effects dominate. The frequency band of the chirp between 16 kHz to 22 kHz sets the wavelength range to approximately 2.2 cm to 1.6 cm, which is close to the distance between reflection points on a person's head, as shown above in Sec. 3.3.3. Proximity to objects increases interference as well, which explains the lower performance in the closer positions ③ and ④, where the projected distance onto the sensor system's aperture between the person and the wall, screen and desk is reduced. If we regard the error distributions of each position in Fig. 6 again, the angles and distances roughly fit non-line-of-sight paths, especially for the Sonogram method.

5.2. Performance

The Direct Intersection method requires less than half the memory for its computations compared to the Sonogram method, as the information is very early condensed in the peak selection part of the algorithm. The index look-up is in itself a cheap operation, but due to the sphere spreading loop to decrease the probability of the algorithm not returning any valid position at all, comes at higher execution duration. The observed worst case for Direct Intersection is with 25 s so high, that no real-time tracking is possible anymore. If we regard Fig. 5c closer, the estimation point gray scale infill is proportional to the inverse spreading factor, so darker colors mean less radial spread before intersecting points could be found. The notion that including strong outliers by allowing the sphere thickness to be spread so far is not confirmed if we consider Fig. 5d.

6. Conclusion

The Sonogram Estimation allows for analysis of room response in more detail and the results are more accurate (i.e. average error) in 3 of 4 observed cases, but inversely the precision (i.e. error variance) of the Direct Intersection is higher in 3 of the cases. The Direct Intersection method allows for less expensive computation by reducing maximum radius spreading, while the Sonogram method's cost can be reduced effectively by limiting the vertical search interval, e.g., to the clutter free area above the desks. For a full range sounding of the room we observed that the locations close to the clutter area are estimated worse regarding, both, accuracy and precision. For a pragmatic operation on hardware with higher memory limitations the Direct Intersection method will perform faster and with similar precision and accuracy, and can be limited in execution time by restricting the sphere radius spreading at the cost of not being able to estimate the position for several intervals. We esteem further investigation into limiting the degradation of the estimation process by single unreliable channels as most promising for improving passive acoustic indoor localization.

Author Contributions: Conceptualization, D.J.S, A.S. and F.H.; methodology, D.J.S., A.S. and J.B.; software, D.J.S and A.S.; validation, D.J.S., A.S., G.F., W.X., A.G. and J.B.; formal analysis, D.J.S. and A.S.; investigation, D.J.S. and A.S.; resources, F.H., K.F., C.S. and S.J.R.; data curation, A.S.; writing—original draft preparation, D.J.S., A.S., G.F., W.X., A.G. and J.B.; writing—review and editing, D.J.S., G.F., W.X. and A.G..; visualization, D.J.S.; supervision, J.B. and F.H.; project administration, F.H., K.F., C.S. and S.J.R.; funding acquisition, F.H., K.F., C.S. and S.J.R. All authors have read and agreed to the published version of the manuscript.

Funding: This work was partially supported by the Fraunhofer Gesellschaft and the state of Baden-Württemberg in the Framework of the MERLIN project, and also the German Ministry of Education and Research (BMBF) under the grant FKZ 16ME0023K ("Intelligentes Sensorsystem zur autonomen Überwachung von Produktionsanlagen in der Industrie 4.0 - ISA4.0").

Institutional Review Board Statement: Not applicable.

Informed Consent Statement: Not applicable.

Data Availability Statement: The data presented in this study are available on request from the corresponding author.

Conflicts of Interest: The funders had no role in the design of the study; in the collection, analyses, or interpretation of data; in the writing of the manuscript, or in the decision to publish the results.

Abbreviations

The following abbreviations are used in this manuscript:

MDPI	Multidisciplinary Digital Publishing Institute
DI	Direct Intersection
DoA	Direction of Arrival
FMCW	Frequency-Modulated Continuous-Wave
LS	Least-Squares
RF	Radio-Frequency
RIR	Room Impulse Response
RSSI	Received Signal Strength Indicator
SONO	Sonogram
SNR	Signal-to-Noise Ratio
TDoA	Time Difference of Arrival
ToF	Time of Flight

References

1. Zafari, F.; Gkelias, A.; Leung, K.K. A Survey of Indoor Localization Systems and Technologies. *IEEE Communications Surveys & Tutorials* **2019**, *21*, 2568–2599. doi:10.1109/COMST.2019.2911558.
2. Rahman, A.B.M.M.; Li, T.; Wang, Y. Recent Advances in Indoor Localization via Visible Lights: A Survey. *Sensors* **2020**, *20*, 1382. doi:10.3390/s20051382.
3. Höflinger, F.; Saphala, A.; Schott, D.J.; Reindl, L.M.; Schindelhauer, C. Passive Indoor-Localization using Echoes of Ultrasound Signals. 2019 International Conference on Advanced Information Technologies (ICAIT), 2019, pp. 60–65. doi:10.1109/AITC.2019.8921282.
4. Pirzada, N.; Nayan, M.Y.; Subhan, F.; Hassan, M.F.; Khan, M.A. Comparative analysis of active and passive indoor localization systems. *AASRI Procedia* **2013**, *5*, 92–97.
5. Caicedo, D.; Pandharipande, A. Distributed Ultrasonic Zoned Presence Sensing System. *IEEE Sensors Journal* **2014**, *14*, 234–243. doi:10.1109/jsen.2013.2282958.
6. Pandharipande, A.; Caicedo, D. User localization using ultrasonic presence sensing systems. 2012 IEEE International Conference on Systems, Man, and Cybernetics (SMC). IEEE, 2012, pp. 3191–3196. doi:10.1109/icsmc.2012.6378282.
7. Caicedo, D.; Pandharipande, A. Transmission slot allocation and synchronization protocol for ultrasonic sensor systems. 2013 10th IEEE International Conference on Networking, Sensing and Control (ICNSC). IEEE, 2013, pp. 288–293. doi:10.1109/icnsc.2013.6548752.
8. Carotenuto, R.; Merenda, M.; Iero, D.; Della Corte, F.G. An Indoor Ultrasonic System for Autonomous 3-D Positioning. *IEEE Transactions on Instrumentation and Measurement* **2019**, *68*, 2507–2518. doi:10.1109/TIM.2018.2866358.
9. Kosba, A.E.; Saeed, A.; Youssef, M. RASID: A robust WLAN device-free passive motion detection system. 2012 IEEE International Conference on Pervasive Computing and Communications. IEEE, 2012. doi:10.1109/percom.2012.6199865.

10. Wang, G.; Gu, C.; Inoue, T.; Li, C. A Hybrid FMCW-Interferometry Radar for Indoor Precise Positioning and Versatile Life Activity Monitoring. *IEEE Transactions on Microwave Theory and Techniques* **2014**, *62*, 2812–2822. doi:10.1109/tmtt.2014.2358572.
11. Bordoy, J.; Schott, D.J.; Xie, J.; Bannoura, A.; Klein, P.; Striet, L.; Höflinger, F.; Häring, I.; Reindl, L.; Schindelhauer, C. Acoustic Indoor Localization Augmentation by Self-Calibration and Machine Learning. *Sensors* **2020**, *20*, 1177. doi:10.3390/s20041177.
12. Pullano, S.A.; Bianco, M.G.; Critello, D.C.; Menniti, M.; La Gatta, A.; Fiorillo, A.S. A Recursive Algorithm for Indoor Positioning Using Pulse-Echo Ultrasonic Signals. *Sensors* **2020**, *20*. doi:10.3390/s20185042.
13. Schott, D.J.; Faisal, M.; Höflinger, F.; Reindl, L.M.; Bordoy Andreú, J.; Schindelhauer, C. Underwater localization utilizing a modified acoustic indoor tracking system. 2017 IEEE 7th International Conference on Underwater System Technology: Theory and Applications (USYS). IEEE, 2017. doi:10.1109/usys.2017.8309451.
14. Chang, S.; Li, Y.; He, Y.; Wang, H. Target Localization in Underwater Acoustic Sensor Networks Using RSS Measurements. *Applied Sciences* **2018**, *8*. doi:10.3390/app8020225.
15. Mrazovac, B.; Bjelica, M.; Kukolj, D.; Todorovic, B.; Samardzija, D. A human detection method for residential smart energy systems based on Zigbee RSSI changes. *IEEE Transactions on Consumer Electronics* **2012**, *58*, 819–824. doi:10.1109/tce.2012.6311323.
16. Retscher, G.; Leb, A. Development of a Smartphone-Based University Library Navigation and Information Service Employing Wi-Fi Location Fingerprinting. *Sensors* **2021**, *21*. doi:10.3390/s21020432.
17. Kaltiokallio, O.; Bocca, M. Real-Time Intrusion Detection and Tracking in Indoor Environment through Distributed RSSI Processing. 2011 IEEE 17th International Conference on Embedded and Real-Time Computing Systems and Applications. IEEE, 2011. doi:10.1109/rtcsa.2011.38.
18. Yigitler, H.; Jantti, R.; Kaltiokallio, O.; Patwari, N. Detector Based Radio Tomographic Imaging. *IEEE Transactions on Mobile Computing* **2018**, *17*, 58–71. doi:10.1109/TMC.2017.2699634.
19. Hillyard, P.; Patwari, N.; Daruki, S.; Venkatasubramanian, S. You're crossing the line: Localizing border crossings using wireless RF links. 2015 IEEE Signal Processing and Signal Processing Education Workshop (SP/SPE). IEEE, 2015. doi:10.1109/dsp-spe.2015.7369561.
20. Suijker, E.M.; Bolt, R.J.; van Wanum, M.; van Heijningen, M.; Maas, A.P.M.; van Vliet, F.E. Low cost low power 24 GHz FMCW radar transceiver for indoor presence detection. 2014 44th European Microwave Conference, 2014, pp. 1758–1761. doi:10.1109/EuMC.2014.6986797.
21. Hnat, T.W.; Griffiths, E.; Dawson, R.; Whitehouse, K. Doorjamb: unobtrusive room-level tracking of people in homes using doorway sensors. Proceedings of the 10th ACM Conference on Embedded Network Sensor Systems - SenSys '12. ACM Press, 2012. doi:10.1145/2426656.2426687.
22. Caicedo, D.; Pandharipande, A. Ultrasonic array sensor for indoor presence detection. Proc. 20th European Signal Processing Conf. (EUSIPCO) 2012, 2012, pp. 175–179.
23. Nishida, Y.; Murakami, S.; Hori, T.; Mizoguchi, H. Minimally privacy-violative human location sensor by ultrasonic radar embedded on ceiling. Proceedings of IEEE Sensors, 2004. IEEE, 2004. doi:10.1109/icsens.2004.1426192.
24. Bordoy, J.; Wendeberg, J.; Schindelhauer, C.; Reindl, L.M. Single transceiver device-free indoor localization using ultrasound body reflections and walls. 2015 International Conference on Indoor Positioning and Indoor Navigation (IPIN). IEEE, 2015. doi:10.1109/ipin.2015.7346965.
25. Mokhtari, G.; Zhang, Q.; Nourbakhsh, G.; Ball, S.; Karunanithi, M. BLUESOUND: A New Resident Identification Sensor—Using Ultrasound Array and BLE Technology for Smart Home Platform. *IEEE Sensors Journal* **2017**, *17*, 1503–1512. doi:10.1109/jsen.2017.2647960.
26. Ribeiro, F.; Florencio, D.; Ba, D.; Zhang, C. Geometrically Constrained Room Modeling With Compact Microphone Arrays. *IEEE Transactions on Audio, Speech, and Language Processing* **2012**, *20*, 1449–1460. doi:10.1109/tasl.2011.2180897.
27. Steckel, J.; Boen, A.; Peremans, H. Broadband 3-D Sonar System Using a Sparse Array for Indoor Navigation. *IEEE Transactions on Robotics* **2013**, *29*, 161–171. doi:10.1109/tro.2012.2221313.
28. Steckel, J. Sonar System Combining an Emitter Array With a Sparse Receiver Array for Air-Coupled Applications. *IEEE Sensors Journal* **2015**, *15*, 3446–3452. doi:10.1109/jsen.2015.2391290.
29. Rajai, P.; Straeten, M.; Alirezaee, S.; Ahamed, M.J. Binaural Sonar System for Simultaneous Sensing of Distance and Direction of Extended Barriers. *IEEE Sensors Journal* **2019**, *19*, 12040–12049. doi:10.1109/jsen.2019.2938971.
30. Zhou, B.; Elbadry, M.; Gao, R.; Ye, F. Towards Scalable Indoor Map Construction and Refinement using Acoustics on Smartphones. *IEEE Transactions on Mobile Computing* **2020**, *19*, 217–230. doi:10.1109/tmc.2019.2892091.
31. Kundu, T. Acoustic source localization. *Ultrasonics* **2014**, *54*, 25–38. doi:10.1016/j.ultras.2013.06.009.
32. Liu, C.; Wu, K.; He, T. Sensor localization with Ring Overlapping based on Comparison of Received Signal Strength Indicator. 2004 IEEE International Conference on Mobile Ad-hoc and Sensor Systems (IEEE Cat. No.04EX975). IEEE, 2004. doi:10.1109/mahss.2004.1392193.
33. Springer, A.; Gugler, W.; Huemer, M.; Reindl, L.; Ruppel, C.C.W.; Weigel, R. Spread spectrum communications using chirp signals. IEEE/AFCEA EUROCOMM 2000. Information Systems for Enhanced Public Safety and Security, 2000, pp. 166–170. doi:10.1109/EURCOM.2000.874794.
34. Milewski, A.; Sedek, E.; Gawor, S. Amplitude Weighting of Linear Frequency Modulated Chirp Signals. Proc. EUROCON 2007 Int. Conf. Comput. Tools, 2007, pp. 383–386. doi:10.1109/EURCON.2007.4400554.

 doi:10.20944/preprints202106.0096.v1

35. Carotenuto, R.; Merenda, M.; Iero, D.; G. Della Corte, F. Simulating Signal Aberration and Ranging Error for Ultrasonic Indoor Positioning. *Sensors* **2020**, *20*. doi:10.3390/s20123548.
36. Saphala, A. Design and Implementation of Acoustic Phased Array for In-Air Presence Detection. Master's thesis, Faculty of Engineering, University of Freiburg, Freiburg, Germany, 2019.
37. MathWorks. ismember. https://de.mathworks.com/help/matlab/ref/double.ismember.html, accessed on 2021-05-27.
38. MathWorks. ind2sub. https://www.mathworks.com/help/matlab/ref/ind2sub.html, accessed on 2021-05-27.
39. MathWorks. smooth. https://de.mathworks.com/help/curvefit/smooth.html, accessed on 2021-05-27.
40. MathWorks. find. https://de.mathworks.com/help/matlab/ref/find.html, accessed on 2021-05-27.